

Imaging neural activity in the ventral nerve cord of behaving adult *Drosophila*

Chin-Lin Chen^{1,2,*}, Laura Hermans^{1,2,*}, Meera C. Viswanathan^{3,4}, Denis Fortun^{5,6},
Michael Unser⁵, Anthony Cammarato^{3,4}, Michael H. Dickinson⁷, Pavan Ramdya^{1,2,‡}

Affiliations:

¹ Brain Mind Institute, École Polytechnique Fédérale de Lausanne, Lausanne, CH-1015, Switzerland

² Interfaculty Institute of Bioengineering, École Polytechnique Fédérale de Lausanne, Lausanne, CH-1015, Switzerland

³ Department of Medicine, Johns Hopkins University, Baltimore, MD 21205, USA

⁴ Department of Physiology, Johns Hopkins University, Baltimore, MD 21205, USA

⁵ Biomedical Imaging Group, École Polytechnique Fédérale de Lausanne, Lausanne, CH-1015, Switzerland

⁶ Signal Processing core of the Center for Biomedical Imaging (CIBM-SP), École Polytechnique Fédérale de Lausanne, Lausanne, CH-1015, Switzerland

⁷ Biology and Biological Engineering, California Institute of Technology, Pasadena, CA 91125, USA

* These authors contributed equally

‡ Correspondence should be addressed to: Pavan.Ramdya@epfl.ch

1 **Abstract**

2 To understand neural circuits that control limbs, one must measure their activity during
3 behavior. Until now this goal has been challenging, because the portion of the nervous
4 system that contains limb premotor and motor circuits is largely inaccessible to large-
5 scale recording techniques in intact, moving animals – a constraint that is true for both
6 vertebrate and invertebrate models. Here, we introduce a method for 2-photon
7 functional imaging from the ventral nerve cord of behaving adult *Drosophila*
8 *melanogaster*. We use this method to reveal patterns of activity across nerve cord
9 populations during grooming and walking and to uncover the functional encoding of
10 moonwalker ascending neurons (MANs), moonwalker descending neurons (MDNs), and
11 a novel class of locomotion-associated descending neurons. This new approach
12 enables the direct investigation of circuits associated with complex limb movements.

13 Introduction

14 Limbs allow animals to rapidly navigate complex terrain, groom, manipulate objects, and
15 communicate. In vertebrates, neural circuits in the spinal cord coordinate the actions of
16 each arm or leg. Circuits within the thorax perform comparable tasks in insects. The
17 thoracic segments of the fruit fly, *Drosophila melanogaster*, house the ventral nerve
18 cord (VNC) which is a fusion of three thoracic and eight abdominal ganglia. The VNC
19 contains six spherical neuromeres, each controlling one leg, a flat dorsal neuropil
20 associated with the neck, wing, and halteres, and a set of intermediate neuropils
21 including the tectulum that may coordinate the action of the legs and wings. Also within
22 the thorax are descending and ascending axons that connect the VNC to the brain run
23 within a pair of neck or cervical connectives, which – like the VNC – are inaccessible in
24 most preparations.

25 In recent years, the VNC of adult *Drosophila* has gained attention as the site
26 where some higher-order decisions are transformed into actions. Adult flies engage in
27 complex limbed behaviors including walking^{1,2}, reaching³, escape jumping⁴, courtship
28 tapping⁵, aggressive boxing⁶, and grooming⁷. Our current understanding of how the
29 VNC coordinates these actions is entirely based on behavioral genetics or recordings
30 from a few neurons in tissue explants⁸, immobilized animals⁹⁻¹¹, or sharp electrode
31 studies in larger insects^{12,13}.

32 To fully understand how VNC circuits orchestrate limb movements, it is
33 necessary to record the activity of individual cells and populations of neurons during
34 behavior. To date, these experiments have not been performed in *Drosophila* due to the
35 difficulty of accessing the VNC in intact, behaving animals. Here we describe a
36 preparation that overcomes this obstacle and makes it possible to record VNC
37 population dynamics in adult animals during walking, grooming, and other actions
38 involving limb movement.

39 Results

40 The VNC lies on the thoracic sternum – a cuticular structure that anchors the leg
41 muscles and the proximal leg segments to the thorax (**Fig. 1a**). Consequently, it is
42 difficult to access the VNC by removing ventral thoracic cuticle without destroying
43 musculoskeletal elements required for limb movement. We chose instead to access the
44 VNC dorsally at the expense of flight-related behaviors¹⁴. This approach requires
45 removing the prescutum and scutum of the dorsal thoracic cuticle, the indirect flight
46 muscles (IFMs), and transecting the proventriculus, crop, and salivary glands of the gut
47 (**Fig. 1a**, see Methods).

48 Using this technique, it is possible to uncover the VNC for functional imaging in
49 flies that are still capable of exhibiting robust behavior, such as walking and grooming,
50 for at least 2-4 hours. To illustrate the extent of VNC access, we drove expression of the
51 genetically encoded calcium indicator, GCaMP6s¹⁵, together with a fiduciary
52 fluorophore, tdTomato¹⁶, throughout the entire nervous system
53 (*GMR57C10>GCaMP6s; tdTomato*)¹⁷, (**Fig. 1b-c** and **Supplementary Video 1**). To
54 perform 2-photon microscopy in semi-intact, behaving animals, we constructed a
55 customized fly holder and spherical treadmill (**Supplementary Fig. 1a**) that, in contrast
56 to previous methods used to record neural activity in the brain^{14,18,19}, permits
57 unobscured optical access to the VNC and videography of leg movements
58 (**Supplementary Fig. 1b**).

59 By focusing on dorsoventral horizontal image planes in animals expressing
60 GCaMP6s and tdTomato pan-neuronally (*GMR57C10>GCaMP6s; tdTomato*), we could
61 record the detailed time course of neural activity in the right and left prothoracic leg
62 neuromeres during walking and grooming (**Fig. 2a-b,e** and **Supplementary Video 2**).
63 We identified two regions-of-interest (ROIs) in the right prothoracic neuromere that
64 correlated with spontaneous prothoracic leg grooming and walking, respectively (**Fig.**
65 **2e**). Alternatively, we could use a piezo-driven microscope objective to acquire coronal
66 x-z image planes. These coronal sections allowed us to simultaneously record activity at
67 different depths of the VNC corresponding to layers housing sensory neuron axons²⁰,
68 interneurons¹¹, and motor neuron dendrites²¹ (Fig. 2a,c; Supplementary Video 3), or

69 monitor activity patterns across populations of descending^{22,23} and ascending
70 fibers^{8,20,23} within the cervical connective (**Fig. 2a,d** and **Supplementary Video 4**).
71 Thus, we confirmed that our new preparation provides optical access to previously
72 inaccessible thoracic neural populations in behaving animals.

73 Using *Drosophila*, it is possible to repeatedly and systematically investigate the
74 functional properties of sparse sets of genetically-identifiable neurons. In one recent
75 study, a thermogenetic activation screen was used to identify a pair of descending
76 neurons – Moonwalker Descending Neurons (MDNs) – which cause flies to walk
77 backwards²³. Additionally, concurrent thermogenetic activation of a set of ascending
78 neurons that project from the VNC to the brain – Moonwalker Ascending Neurons
79 (MANs) – resulted in even more sustained backwards walking, perhaps by arresting
80 forward walking²³. While these activation experiments show that these neurons play an
81 important role in the control of backwards walking, their native activity patterns and the
82 means by which they regulate and report limb movements remain unknown.

83 Because MAN and MDN axons terminate in the gnathal ganglia (GNG) and the
84 VNC, which are both relatively inaccessible regions of the nervous system, it is difficult
85 to record the activity of these cells during any behavior. We used our functional imaging
86 approach to overcome this challenge and recorded the activity of this set of ascending
87 and descending interneurons within the VNC. Because of the vertical movement
88 artifacts associated with walking, we imaged the activity of MAN axons through coronal
89 sections within the cervical connective (**Fig. 3a**). With this approach, axons are visible
90 as small ellipses (**Fig. 3b**). The *MAN* split-GAL4 line we used drives expression in a pair
91 of dorsal and a pair of ventral neurons. We focused our analysis on the dorsal pair of
92 neurons – hereafter referred to as dMANs – because they showed conspicuous
93 changes in activity (**Fig. 3c**). The activity of left and right dMANs were strongly
94 correlated (**Supplementary Fig. 2a**; Pearson's $r = 0.96 \pm 0.01$, $n = 5$ flies), allowing us
95 to study their collective response properties. Specifically, we automatically identified the
96 occurrence of transient increases in dMAN fluorescence – referred to as 'events' – and
97 examined the corresponding behavioral changes reflected in the spherical treadmill data
98 (see Methods). Our analysis revealed that dMAN events were associated with rapid
99 bimodal anterior-posterior rotations of the spherical treadmill (**Fig. 3d**, $n = 746$ left and

100 748 right dMAN events from 9773 s of data from 5 flies). By close inspection of the
101 video data, we observed that these rotations occur when flies extend all six legs to push
102 down on the ball (**Supplementary Videos 5 and 6**).

103 Next, we asked to what extent MDNs are active during periods of backwards
104 walking, a possibility suggested by behavioral responses to thermogenetic²³ or
105 optogenetic²⁴ MDN stimulation. To address this question, we applied our approach of
106 imaging coronal sections of the thoracic cervical connective using MDN driver line flies
107 expressing GCaMP6s and tdTomato (*MDN-1>GCaMP6s; tdTomato*)(**Fig. 4a-b**). As for
108 dMANs, the activity of pairs of MDNs were strongly correlated (**Fig 4c**), allowing us to
109 focus on their collective response properties (**Supplementary Fig. 2b**; Pearson's $r =$
110 0.93 ± 0.001 , $n = 3$ flies). As predicted, MDNs were active prior to anterior rotations of
111 the spherical treadmill, corresponding to brief episodes of backward walking (**Fig. 4c-d**,
112 $n = 900$ left and 900 right MDN events from 3 flies and 7790 s of data; **Supplementary**
113 **Videos 7 and 8**).

114 In addition to resolving the functional properties of previously identified neurons,
115 our method facilitates the discovery of novel cell classes that are active during walking,
116 grooming, and other behaviors involving the limbs or abdomen. As a proof-of-concept,
117 we selected four split-GAL4 lines²⁵ that drive sparse expression in pairs of descending
118 neurons²² whose axons project to leg neuromeres in the VNC (classes DNa01, DNb06,
119 DNg10, and DNg13). Among these, we found that DNa01 neurons – hereon referred to
120 as A1 cells – were active in a manner that was clearly linked to locomotor state
121 (*A1>GCaMP6s; tdTomato*)(**Fig. 5a-b** and **Supplementary Video 9**). The activity of left
122 and right A1 neurons were not highly correlated (**Fig. 5c** and **Supplementary Fig. 2c**;
123 Pearson's $r = 0.53 \pm 0.17$, $n = 4$ flies). Therefore, we investigated the response
124 properties of the left and right cells separately. We found that although the activities of
125 both cells are linked to forward walking, events associated only with left A1 activity were
126 correlated with positive medial-lateral and yaw rotations, or rightward turning by the fly
127 (**Fig. 5d** and **Supplementary Video 10**; $n = 1644$ events from 4 flies and 8784 s of
128 data). As expected from bilateral symmetry, activity in the right A1 neuron coincided
129 with negative medial-lateral and yaw rotations, or leftward turning (**Fig. 5e** and
130 **Supplementary Video 11**; $n = 1651$ events from 4 flies and 8784 s of data).

131 This approach for recording neural activity in the VNC of behaving *Drosophila*
132 opens up many new avenues for studying premotor and motor circuits. Nevertheless,
133 we can imagine further improvements that will accelerate the study of the thoracic
134 nervous system. For example, in our preparation we found it challenging and time-
135 consuming to remove the indirect flight muscles (IFMs) which fill most of the thorax.
136 Although large, these muscles are quite fragile and tend to disintegrate over the course
137 of an hour after the cuticle of the notum is removed. To increase the efficiency of our
138 dissection, we devised a transgenic strategy to selectively ablate IFMs. We drove the
139 expression of Reaper – a protein promoting apoptosis²⁶ – in the IFMs by using a 5'
140 *Act88F* promotor sequence²⁷. *Act88F:Rpr* animals show a nearly complete loss of the
141 IFMs after 7 days post-eclosion (dpe) when raised at 25°C (**Fig. 6a-b**). This loss results
142 in highly elevated or slightly depressed wings, phenotypes identical to those seen in
143 IFM developmental mutants²⁸. The heterozygous *Act88F:Rpr* transgenic background
144 greatly accelerated the dorsal thoracic dissection. Although the imaging data in this
145 manuscript were performed without the *Act88F:Rpr* transgene, we envisage that this
146 genetic reagent will greatly simplify and accelerate use of this method in the
147 neuroscience community.

148 Here we have described a new preparation that enables the visualization of
149 genetically identified neurons in the VNC and cervical connective of *Drosophila* during
150 behavior. We can record the activity of entire neural populations (**Fig. 2**) or measure the
151 encoding of known (**Figs. 3 and 4**) and novel sparse cell classes (**Fig. 5**). This method
152 fills a critical gap in the study of sensory-motor pathways and serves as a complement
153 to ongoing genetic behavioral screens^{23,29,30} aimed at elucidating how populations of
154 neurons coordinate limb movements and orchestrate a variety of legged behaviors.

155

156 **Methods**

157 ***Drosophila* lines**

158 Several lines (*GMR57C10-Gal4*, *UAS-GCaMP6s*, *UAS-GCaMP6f*, *UAS-CD4:tdGFP*,
159 and *UAS-tdTomato*) were obtained from the Bloomington Stock Center. *MAN-Gal4*
160 (*VT50660-AD*; *VT14014-DBD*) and *MDN-1-Gal4* (*VT44845-DBD*; *VT50660-AD*) were
161 provided by B. Dickson (Janelia Research Campus). *DNa01-Gal4* (SS00731:

162 *GMR22C05-AD; GMR56G08-DBD*), *DNb06-Gal4* (SS02631: *GMR20C04-AD;*
163 *BJD113E03-DBD*), *DNg13-Gal4* (SS02538: *BJD118A10-AD; BJD123E03-DBD*), and
164 *DNg16-Gal4* (SS01543: *BJD104A07-AD; BJD107F12-DBD*) were provided by G. Rubin
165 (Janelia Research Campus). Transgenic *Actin88F:Rpr* strains (*Act88F:Rpr* flies) were
166 generated using an *Actin88F:eGFP* construct described previously²⁷ and injected
167 (BestGene, Chino Hills, CA, USA) with the phiC31-based integration system using the
168 attP18 (X chromosome) landing site³¹.

169

170 **Fluorescence imaging of indirect flight muscles**

171 Fluorescent microscopy of hemi-thoraces was performed as described previously^{32,33}.
172 Briefly, flies were anesthetized and their heads and abdomens were then removed.
173 Thoraces were fixed overnight in 4% paraformaldehyde at 4°C and rinsed in 1x
174 phosphate buffered saline (PBS) the following day. The specimens were arranged on a
175 glass slide, snap frozen in liquid nitrogen and bisected down the midsagittal plane using
176 a razor blade. IFMs were stained with Alexa-Fluor 568 Phalloidin (1:100 in PBS with
177 0.1% Triton-X (PBST)) overnight at 4°C, rinsed with PBS and visualized using EVOS®
178 FL Cell Imaging System (Life Technologies) at 4X magnification. For whole-mount
179 imaging of IFM myofibrils, flies were prepared and thoraces bisected as described
180 above. Hemi-thoraces were stained with Alexa-Fluor 568 phalloidin (1:100 in PBST)
181 overnight at 4°C. Samples were rinsed in PBS, mounted with Vectashield (Vector
182 Laboratories) and visualized using a Leica TCS SPE RGBV confocal microscope (Leica
183 Microsystems) at 100X magnification.

184

185 **Immunofluorescence imaging of whole-mount brains and ventral nerve cords**

186 Brains and ventral nerve cords (VNCs) were dissected out of 2-3 dpe female flies in
187 PBS. Tissues were then fixed for 20 minutes in 4% paraformaldehyde in PBS at room
188 temperature. After fixation, brains and VNCs were washed 2-3 times in PBS with 1%
189 Triton-X-100 (PBST) and then incubated at 4°C overnight in PBST. Samples were then
190 placed in PBST with 5% normal goat serum (PBSTS) for 20 min at room temperature.
191 They were then incubated with primary antibodies (rabbit anti-GFP at 1:500,
192 ThermoFisher; mouse anti-Bruchpilot/nc82 at 1:20, Developmental Studies Hybridoma

193 Bank) diluted in PBSTS for 48 h at 4°C. Brains and VNCs were rinsed 2-3 times in
194 PBST for 10 min each before incubation with secondary antibodies (goat anti-rabbit
195 secondary antibody conjugated with Alexa 488 at 1:500; Thermofisher; goat anti-mouse
196 secondary antibody conjugated with Alexa 633 at 1:500; Thermofisher) diluted in
197 PBSTS for 48 h at 4 °C. Finally, brains and VNCs were rinsed 2-3 times for 10 min each
198 in PBST and mounted onto slides with bridge coverslips in Slowfade mounting-media
199 (Thermofisher).

200 Samples were imaged using a Carl Zeiss LSM 700 Laser Scanning Confocal
201 Microscope with the following settings: 20X magnification, 8-bit dynamic range, 2x
202 image averaging, 0.52 × 0.52 μm pixel size, 0.57 μm z-axis interval. Standard deviation
203 z-projections of imaging volumes were made using Fiji³⁴.

204

205 **Thoracic dissection for ventral nerve cord imaging**

206 Custom holders used to mount flies during imaging were fabricated as described
207 previously³⁵. For VNC imaging, these stages were modified to have (i) flat rather than
208 folded frames, and (ii) chamfered vertices to make the spherical treadmill visible to optic
209 flow sensors (Shapeways, <https://www.shapeways.com/model/upload-and-buy/5963553>).

211 All experiments were performed on 1-3 dpe female flies raised at 25°C on
212 standard cornmeal food on a 12 h light:12 h dark cycle. Flies were anaesthetized at 4°C.
213 A female fly was selected and, in some cases, its wings were clipped to simplify the
214 mounting process. The fly's dorsal thorax was then pushed through a hole in the steel
215 shim of a custom imaging stage. The stage was then flipped over, UV-curing glue
216 (Bondic, Aurora, ON Canada) was carefully applied around the perimeter of the thorax
217 and hardened through UV illumination (LED-200, Electro-Lite Co. Bethel, CT USA). UV
218 glue was then similarly applied to fix the head and abdomen to the underside of the
219 stage. The stage was then filled with extracellular saline as described previously¹⁴.
220 Under a high-magnification dissection microscope (Leica M165C), a hypodermic needle
221 (30G, BD PrecisionGlide, Franklin Lakes, NJ USA) was used to slice and lift the cuticle
222 off of the dorsal thorax³⁶, being careful not to sever the neck connective. Subsequently,
223 in non-*Act88F:Rpr* animals, a pair of dull forceps was used to remove IFMs,

224 predominantly from the anteriomedial region of the thorax overlying the proventriculus
225 (this step is unnecessary in aged *Act88F:Rpr* animals). This process exposes the dorsal
226 surface of the proventriculus – a large bulbous structure in the gut. With great care, a
227 pair of super-fine forceps was used to grasp and lift the proventriculus to displace much
228 of the gut (including the crop and salivary glands) from the more ventrally located
229 nervous system. With the gut thus elevated, ultra-fine clipper scissors (Fine Science
230 Tools, Foster City, CA USA) were used to transect it at its anterior-most section. The
231 proventriculus was then peeled back and a posterior incision was made to completely
232 remove these portions of the gut, fully revealing the underlying nervous tissue. In some
233 cases, we observed that gut or muscle tissue would begin to obscure the VNC during
234 imaging. Therefore, loose tissue should be removed at this stage while taking great care
235 not to sever the VNC. After each dissection, we examined the extent to which the
236 animal moved its legs in response to a puff of air. This proved to be an accurate
237 predictor of the success of the preparation.

238

239 **2-photon microscopy during behavior**

240 Experiments were performed in the evening zeitgeber time (Z.T.) and animals were
241 typically imaged 30-60 min following dissection. We found that individual animals
242 provided useful data for 2-4 h. Fly holders were secured to a platform raised over the
243 spherical treadmill (**Supplementary Fig. 2a**). The VNC was located using microscope
244 oculars and then aligned to the center of the field-of-view using 2-photon microscopy.

245 The spherical treadmill was an aluminum rod with a ball-shaped hole milled near
246 its tip¹⁸. We fabricated 10 mm diameter foam balls (Last-A-Foam FR-7106, General
247 Plastics, Burlington Way, WA USA) and manually spotted them using a Rapidograph
248 pen (Koh-I-Noor, Leeds, MA USA) to provide high-contrast features for optic flow
249 measurements. A 500-600 mL/min stream of filtered and humidified air was passed
250 through the holder using a digital flow controller (Sierra Instruments, Monterey, CA
251 USA). Movements of the ball were measured using optical flow sensors (ADNS3080)
252 outfitted with zoom lenses (Computar MLM3X-MP, Cary, NC USA). The ball and fly
253 were illuminated using a pair of IR LEDs (850-nm peak wavelength) coupled to optic
254 fibers and collimator lenses (ThorLabs, Newton, NJ USA). Optic flow measurements

255 were passed to a microcontroller board (Arduino Mega2560) to be recorded using
256 custom-written Python code. Simultaneously, videography of behaviors on the ball were
257 made using an IR-sensitive firewire camera (Basler, Ahrensburg, Germany) at
258 approximately 30 frames per second.

259 We performed 2-photon microscopy using a Bergamo II microscope (ThorLabs)
260 outfitted with two GaAsP PMT detectors for GCaMP6 and tdTomato imaging,
261 respectively, and coupled to a Ti:Sapphire laser (MaiTai DeepSee, Newport Spectra-
262 Physics, Santa Clara, CA USA) tuned to 930 nm. We used an Olympus 20X objective
263 water-immersion lens with 1.0 NA (Olympus, Center Valley, PA USA). The microscope
264 was controlled using ThorImage software (ThorLabs). Occasionally, a puff of air was
265 used to elicit walking behaviors. These puffs were digitally encoded (Honeywell AWM
266 3300V, Morris Plains, NJ USA). Custom ROS software interfaced through an analog
267 output device (Phidgets, Calgary, Canada) to ThorSync software (ThorLabs) was used
268 to synchronize optic flow measurements, behavior videography, air puff measurements,
269 and 2-photon image acquisition. For coronal section imaging, a piezo collar (Physik
270 Instrumente, Karlsruhe, Germany) was used for rapid z-axis movements of the
271 microscope objective lens.

272

273 **Data analysis**

274 We analyzed all data using custom scripts written in Python. Because the data
275 acquisition frequency differed for optic flow, behavior videography, and 2-photon
276 imaging we interpolated signals to that of the highest frequency. Subsequently, optic
277 flow data were smoothed using a running average and then translated into rotations s^{-1}
278 for the anterior-posterior, medial-lateral, and yaw axes as described in¹⁸.

279

280 *Pan-neuronal image registration, ROI identification, and fluorescence processing*
281 *(related to Fig. 2)*

282 We observed that large tissue deformations could occur during behavior. Therefore, we
283 performed post-hoc registration of pan-neuronal imaging data. To do this, we registered
284 all frames of an imaging experiment with one reference image. Because the complexity
285 of the deformations could not be captured by simple parametric motion models (e.g.,

286 affine transformations), we used a non-parametric, variational approach, designed to
287 model arbitrarily complex deformations. We computed the motion field \mathbf{w} between the
288 reference image, denoted I_r , and the image at time t , denoted I_t , by solving the
289 minimization problem

290

$$\hat{\mathbf{w}} = \arg \min_{\mathbf{w}} D(\mathbf{w}) + \lambda \sum_{\mathbf{x} \in \Omega} \|\nabla \mathbf{w}(\mathbf{x})\|_2^2, \quad (1)$$

291

292 where $D(\mathbf{w})$ is a data fitting term, the second term is a regularization promoting
293 smoothness of \mathbf{w} by penalizing its gradient $\nabla \mathbf{w}$ ³⁷, Ω is the discrete image domain, and
294 the parameter λ weights the contributions of the two terms.

295 The sequence tagged with GCaMP6s images is characterized by two main
296 difficulties for motion estimation. First, fast motion of the fly induces very large
297 deformations. Second, the activation of neurons produces large local intensity changes
298 between corresponding pixels in I_r and I_t . To address these issues, we defined a data
299 term of the form

300

$$D(\mathbf{w}) = \rho(\mathbf{w}, I_r, I_t) + \gamma \phi(\mathbf{w}, J_r, J_t). \quad (2)$$

301

302 The first term models the standard assumption of conservation of intensity along the
303 trajectory of each pixel. It is defined by

304

$$\rho(\mathbf{w}, I_r, I_t) = \sum_{\mathbf{x} \in \Omega} |I_t(\mathbf{x} + \mathbf{w}(\mathbf{x})) - I_r(\mathbf{x})|, \quad (3)$$

305

306 where we use an ℓ_1 norm to gain partial robustness to intensity changes³⁸. The second
307 term in (2) is a feature matching constraint inspired by Revaud and co-workers³⁹, written
308 as

309

$$\phi(\mathbf{w}, J_r, J_t) = \sum_{\mathbf{x} \in \Omega} \|\mathbf{w}(\mathbf{x}) - \mathbf{m}(\mathbf{x}, J_r, J_t)\|_1, \quad (4)$$

310

311 where the images J_r and J_t are the analog of I_r and I_t in the second channel tagged
312 with tdTomato, for which we do not expect activity-dependent intensity changes.
313 Minimizing the function ϕ favors motion vectors $\mathbf{w}(\mathbf{x})$ to be close to feature
314 correspondences $\mathbf{m}(\mathbf{x}, J_r, J_t)$, computed on a sparse set of relevant keypoints. We obtain
315 \mathbf{m} with the feature matching algorithm proposed by Revaud and co-workers³⁹, which is
316 specifically designed to handle large image deformations. We compute \mathbf{m} using J_r and
317 J_t , such that the correspondences are also insensitive to the intensity changes between
318 I_r and I_t . As a result, the estimation is guided by reliable feature matches. We found
319 that it is necessary to keep a standard data term (3) defined on the GCaMP6s imaging
320 channel, because the tdTomato channel may not provide information in some regions of
321 the image. The parameter γ balances the two terms in (2).

322 We solved the optimization problem (1) with an alternated direction method of
323 multiplier (ADMM) algorithm⁴⁰. We introduced two splitting variables, associated with the
324 regularization and the feature matching terms, respectively. Each sub-problem of the
325 algorithm was solved analytically. We used parts of the inverse problems library
326 described in⁴¹. A post processing based on weighted median filtering was applied with
327 the method of⁴².

328 From these registered imaging data, regions-of-interest (ROIs) were manually
329 selected. $\% \Delta F/F$ values were then calculated from fluorescence signals averaged within
330 the ROIs. $\Delta F = F_t - F$, where F_t is the average fluorescence within an ROI at time, t . F is
331 a baseline fluorescence signal that was calculated as the average pixel value for the
332 first ten sequential GCaMP6s images for which no cellular activity was observed (i.e.,
333 minimal and unchanging GCaMP6s fluorescence).

334

335 *Sparse neuron ROI identification, and fluorescence processing (related to Figs. 3-5)*

336 For single-neuron fluorescence data, ROIs were selected using custom Python scripts
337 relying on OpenCV and Numpy libraries. First, a reference frame was selected for which
338 software identified all potential ROIs. To do this, the GCaMP6s channel image was
339 smoothed to reduce background noise and then an Otsu filter threshold was applied to
340 the image. An erosion factor was then applied on all objects detected within the image.

341 Contours of all detected objects were then presented to the user for manual selection.
342 Once these reference ROIs were selected for left and right neurons, we used a cross-
343 correlation-based image registration algorithm⁴³ to identify the most likely left and right
344 ROIs for each image frame based on those manually selected on the reference frame.
345 A second script was used to manually verify automatically selected ROIs and, if
346 incorrect, to display all potential ROIs within the frame for manual selection. If chosen
347 erosion values yielded malformed ROI shapes, another script was used to manually
348 position elliptical ROIs with arbitrary orientations on a given frame. Finally, binary ROI
349 images were used as an image mask to extract mean fluorescence intensities from the
350 original GCaMP6s or tdTomato images. These signals were reported as $\% \Delta R/R$ as in⁴⁴
351 to reduce the effects of motion artifacts on fluorescence signals. Due to the absence of
352 stimuli for eliciting behaviors, the baseline R was calculated as the minimum ratio of
353 GCaMP6s / tdTomato within a 2.5 s bin.

354 To detect transient increases in activity above the $\% \Delta R/R$ baseline, we
355 developed an algorithm based partly on⁴⁵. We first determined when the first order
356 derivative of the $\% \Delta R/R$ signal crossed an arbitrary threshold, which was calculated as
357 a percentile determined by examining all derivatives values for a given neuron class
358 (i.e., MDN, MAN, or A1). We reasoned that threshold values should be characteristic
359 and potentially different for each neuron class because fluorescence dynamics are
360 related to intrinsic physiological properties that can differ across neuron classes but not
361 across experiments investigating a single class. We set this threshold for the derivative
362 value as the 97.5th percentile for MDNs and dMANs and 90th percentile for A1 neurons.
363 A lower threshold value was selected for A1 neurons because many more fluorescence
364 transients were observed in A1 $\% \Delta R/R$ fluorescence traces. These transients would be
365 overlooked using the 97.5th percentile. To identify the onset of fluorescence increases
366 we found the nearest preceding time point where the derivative crossed zero (i.e.,
367 typically an inflection between decreases and increases in fluorescence). This zero-
368 crossing is considered the time-point of an 'event' associated with the identified
369 fluorescence increase. Events detected close to one another with no intervening
370 derivative zero-crossing were compressed into one event associated with the first time
371 point. There were ~10 separate experiments per animal. Events in the first and last 10 s

372 of each experiment were not considered since the window for data presentation
373 encompassed 10 s before and 10 s after each event.

374 Because left and right MDN and dMAN cells strongly covaried (**Supplementary**
375 **Fig. 2**), an additional step was performed for event detection: if events were detected in
376 both left and right neurons within 2 s of one another, both events were retained;
377 otherwise, an event identified for neuron A (e.g., left MDN) and not neuron B (e.g., right
378 MDN) was also added to neuron B's event library.

379 By contrast, left and right A1 neural activities did not strongly covary. Therefore,
380 analyzed events associated uniquely to one and not the other neuron. To accomplish
381 this, if an event was detected in both left and right A1 neurons within a time window of
382 0.25 s, neither of the events were logged for analysis.

383 $\% \Delta R/R$ and optic flow traces linked to each event were aligned by setting the
384 event time points to 0 s. We then computed the mean and bootstrapped 95%
385 confidence intervals for these aligned traces using the Python Seaborn library. Optic
386 flow and $\% \Delta R/R$ measurements were downsampled to 500 values/s for this analysis. To
387 increase clarity, $\% \Delta R/R$ traces were baseline-subtracted to make them zero at the time
388 of the event in the summary **Figs. 3d, 4d, and 5d-e**. Control shuffled data (gray traces)
389 were computed by instead assigning random time-points in place of real, identified
390 events. These random time points were treated as real events and their mean and
391 bootstrapped 95% confidence intervals were computed and plotted for comparison.

392

393 *Covariance analysis (related to Supplementary Figure 2)*

394 Covariance analysis was performed with a custom Python script using Matplotlib and
395 Numpy libraries. Scatter plots were computed comparing left and right neuron $\% \Delta R/R$
396 values from all experiments for each fly separately. All data were included for analysis in
397 these scatter plots with the exception of two MDN flies that exhibited unusually low
398 fluorescence values. Pearson's r values are reported as mean \pm standard deviation.

399

400 *Event-related behaviors (related to Supplementary Videos 6, 8, 10, and 11)*

401 Events chosen for behavioral summary videos were chosen from automatically detected
402 events as described above. For dMANs, events were manually selected from those that

403 maximized the difference in anterior-posterior ball rotations between 1 s before the
404 event and 2 s after the event. For MDNs, events were manually selected from among
405 those that minimized anterior-posterior ball rotations up to 2 s after the event. For A1
406 neurons, events were manually selected from among those that maximized the average
407 yaw ball rotations (positive for left A1 neuron examples and negative for right A1 neuron
408 examples) for up to 2 s after the events.

409 **Acknowledgments**

410 We thank B.J. Dickson (Janelia Research Campus, VA) for *MDN-1-Gal4* and *MAN-Gal4*
411 fly strains. We thank G. Rubin (Janelia Research Campus, VA) for *DNa01-Gal4*,
412 *DNb06-Gal4*, *DNg13-Gal4*, and *DNg16-Gal4* fly strains. AC acknowledges support from
413 the National Institutes of Health (R01HL124091). MHD acknowledges support from the
414 National Institute of Neurological Disorders and Stroke of the National Institutes of
415 Health (U01NS090514). PR acknowledges support from the Swiss National Science
416 Foundation (31003A_175667).

417

418 **Author contributions**

419 C.L.C. generated strains; performed experiments; analyzed data

420 L.H. analyzed data

421 M.C.V. performed experiments; analyzed data

422 D.F. wrote analysis code

423 M.U. supervised the project

424 A.C. designed and supervised the project

425 M.H.D. designed and supervised the project

426 P.R. conceived of, designed, and supervised the project; performed experiments;
427 analyzed data

428 All authors contributed to writing the paper

429

430 **Competing financial interests**

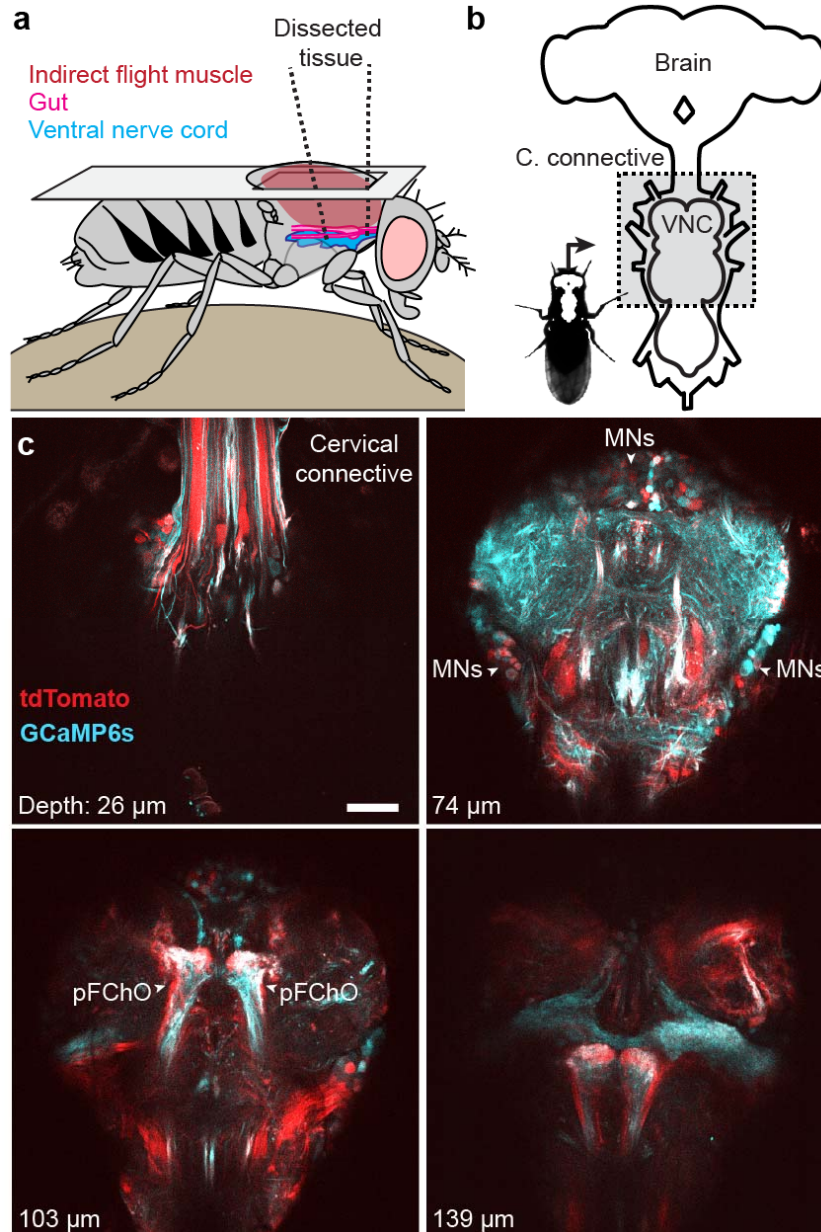
431 The authors declare no competing financial interests.

432

433 **Corresponding author**

434 Correspondence should be addressed to: Pavan Ramdya (Pavan.Ramdya@epfl.ch)

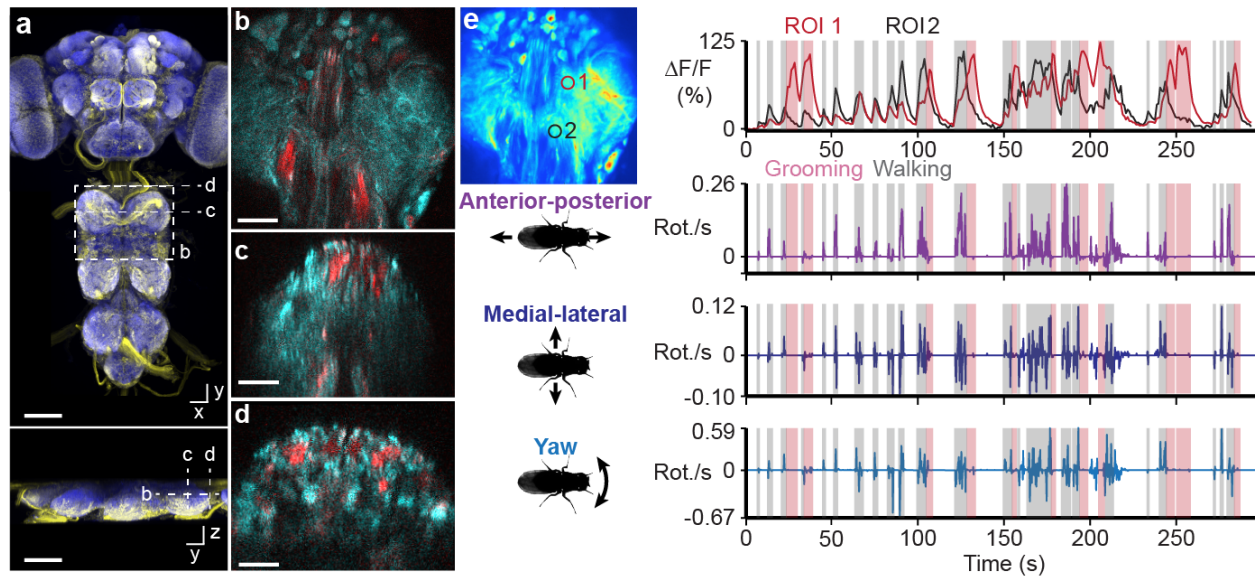
435 **Figure Legends**



436

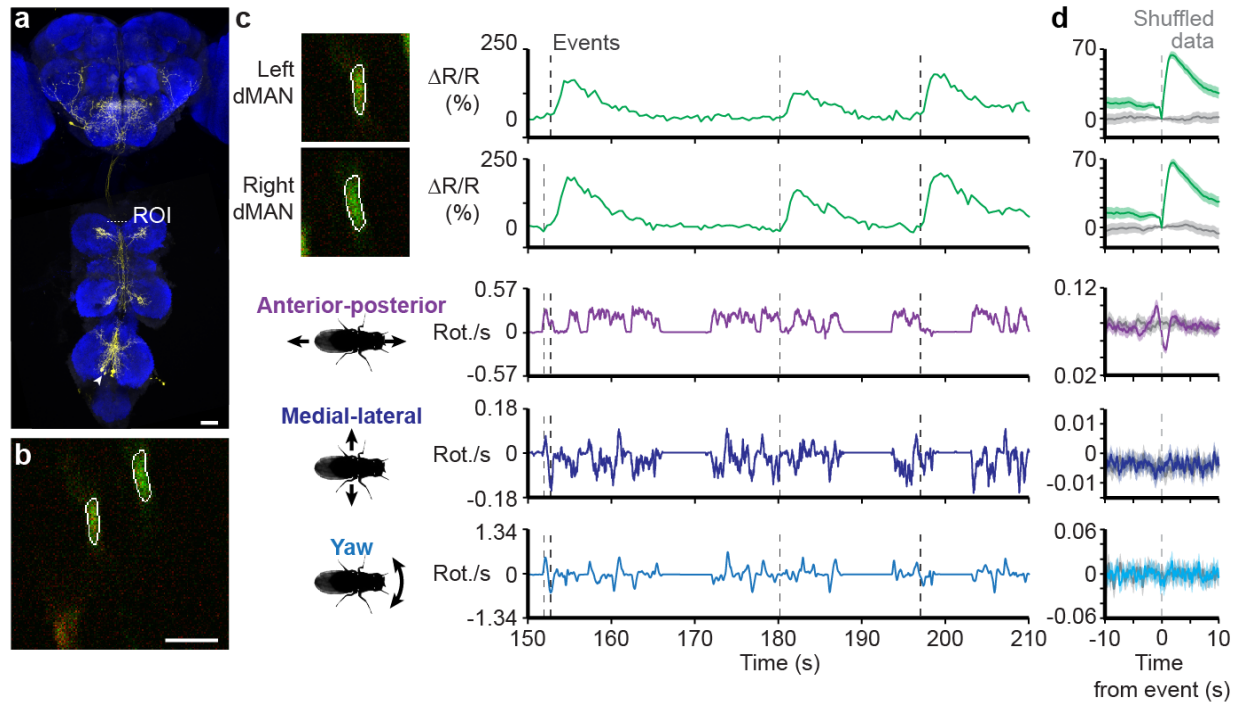
437 **Figure 1 | Dissection for imaging the adult *Drosophila* ventral nerve cord (VNC).**

438 **(a)** Schematic of the dorsal thoracic dissection. **(b)** Overview of newly accessible
439 nervous tissue following the thoracic dissection. **(c)** Horizontal sections of the VNC
440 imaged at different depths in an animal expressing GCaMP6s (cyan) and tdTomato
441 (red) throughout the nervous system (*GMR57C10>GCaMP6s; tdTomato*). Motor
442 neurons (MNs) and prothoracic (pFChO) femoral chordotonal organs are indicated by
443 white arrowheads. Scale bar is 30 μm.



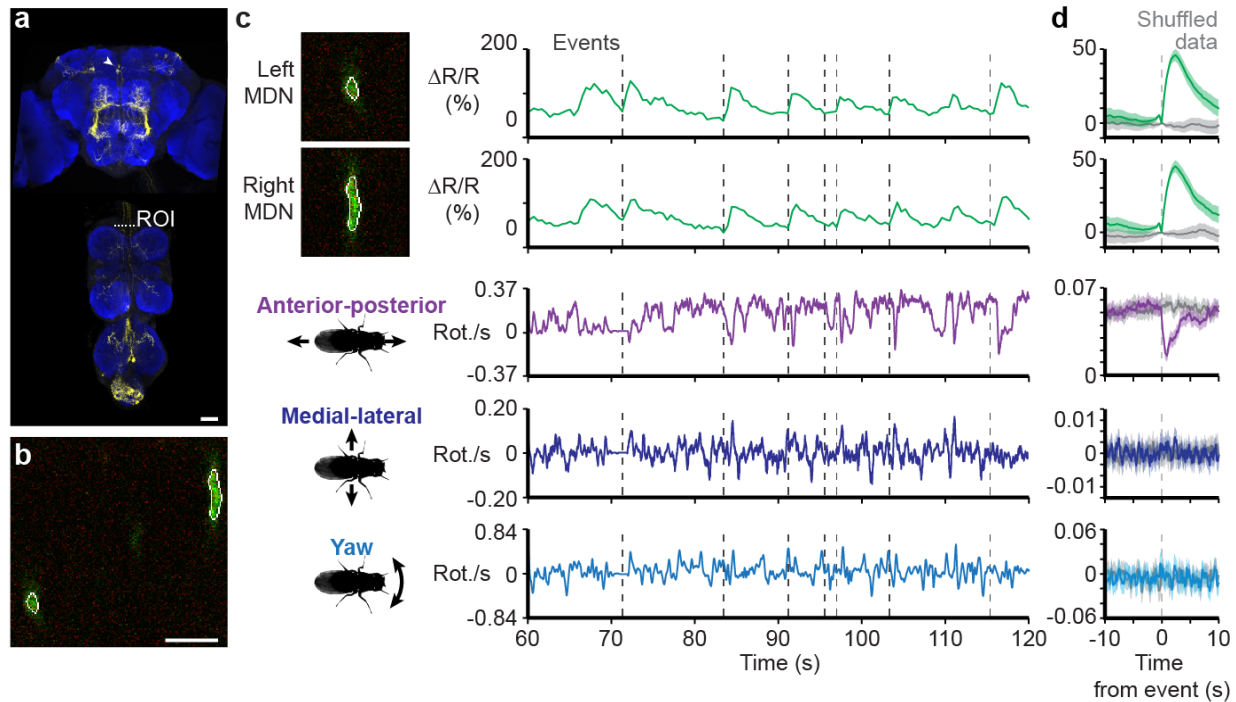
444

445 **Figure 2 | Recording populations of neurons in the VNC during behavior. (a)**
446 Confocal image of pan-neuronal driver line expression in the brain and VNC. Scale bars
447 are 90 μm . Neuronal GFP (yellow) and neuropil (nc82, blue) are labelled. Dashed lines
448 highlight the imaging modalities made possible by thoracic dissection: **(b)** horizontal
449 section imaging of the VNC (scale bar is 35 μm), **(c)** coronal section imaging of the VNC
450 (scale bar is 50 μm), and **(d)** coronal section imaging of the cervical connective (scale
451 bar is 35 μm). All three modalities are illustrated by imaging flies expressing GCaMP6s
452 and tdTomato throughout the nervous system (*GMR57C10>GCaMP6s; tdTomato*). **(e)**
453 % $\Delta F/F$ image of a VNC horizontal section of the same animal in **(b)**. ROI-associated
454 fluorescence signals during walking (gray) and grooming (pink) are shown on the top-
455 right. Corresponding rotations of the spherical treadmill are shown on the bottom-right.



456

457 **Figure 3 | Recording the activity of dorsal Moonwalker Ascending Neurons**
 458 **(dMANs) during behavior. (a)** Confocal image of *MAN-Gal4* driver line expression in
 459 the brain and VNC (scale bar is 40 μm). Neuronal GFP (yellow) and neuropil (nc82,
 460 blue) are labelled. A dashed white line highlights the x-z plane imaged. **(b)** Coronal
 461 section of the thoracic cervical connective in an animal expressing GCaMP6s and
 462 tdTomato in MANs (*MAN>GCaMP6s; tdTomato*). Scale bar is 3.5 μm . **(c)** Separated
 463 ROIs **(top-left)** and associated fluorescence signals from left and right dMANs **(top-**
 464 **right)**. Corresponding rotations of the spherical treadmill are shown on the bottom right.
 465 Events are indicated as dashed gray lines. **(d)** Summary of dMAN activity and spherical
 466 treadmill rotations with respect to fluorescence events aligned to 0 s (dashed gray line).
 467 Control data in which events are time-shuffled are overlaid in grey. Shown are the
 468 means (solid line) and bootstrapped 95% confidence intervals (transparencies).



469

470 **Figure 4 | Recording the activity of Moonwalker Descending Neurons (MDNs)**

471 **during behavior. (a)** Confocal image of *MDN-1-Gal4* driver line expression in the brain

472 and VNC (scale bar is 40 μ m). Neuronal GFP (yellow) and neuropil (nc82, blue) are

473 labelled. A dashed white line highlights the x-z plane imaged. **(b)** Coronal section of the

474 thoracic cervical connective in an animal expressing GCaMP6s and tdTomato in

475 Moonwalker Descending Neurons (*MDN-1>GCaMP6s; tdTomato*). Scale bar is 6 μ m.

476 **(c)** Separated ROIs (**top-left**) and associated fluorescence signals from left and right

477 MDNs (**top-right**). Corresponding rotations of the spherical treadmill are shown on the

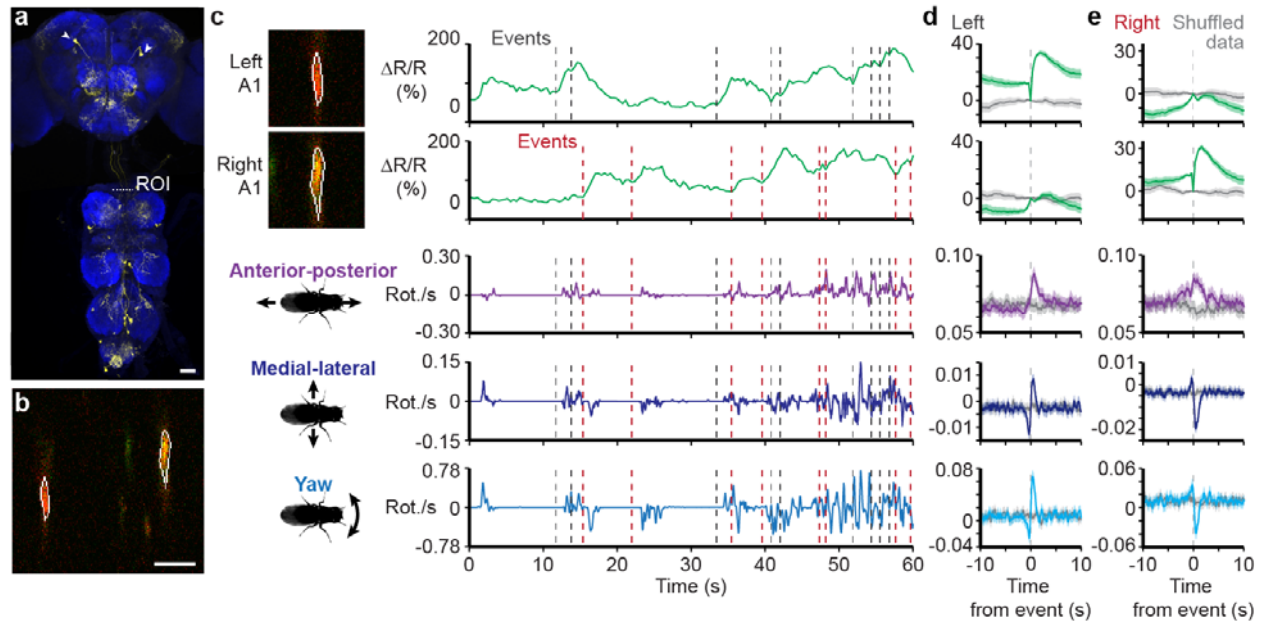
478 bottom right. Events are indicated as dashed gray lines. **(d)** Summary of MDN activity

479 and spherical treadmill rotations with respect to fluorescence events aligned to 0 s

480 (dashed gray line). Control data in which events are time-shuffled are overlaid in grey.

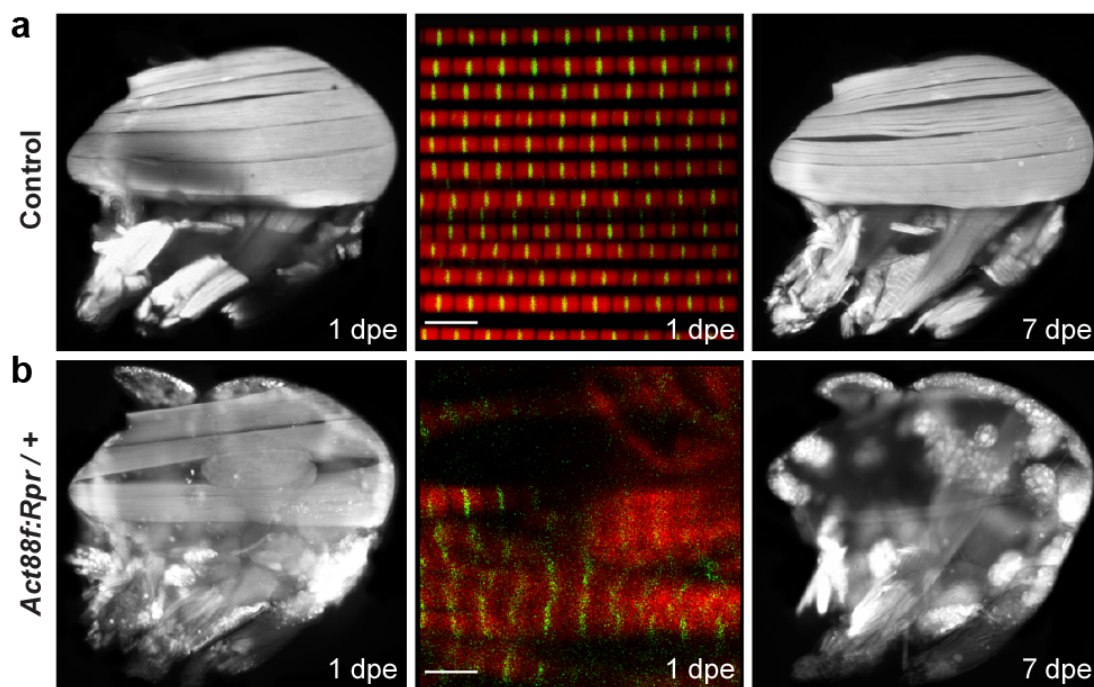
481 Shown are the means (solid line) and bootstrapped 95% confidence intervals

482 (transparencies).



483

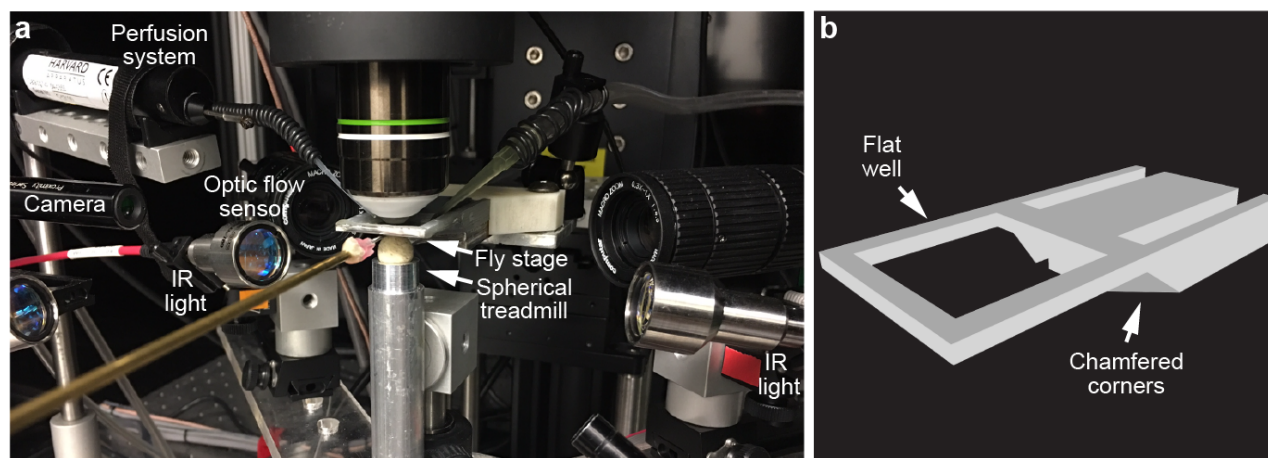
484 **Figure 5 | Recording the activity of A1 neurons during behavior. (a)** Confocal image
485 of *DN0a1-Gal4* driver line expression in the brain and VNC (scale bar is 40 μ m).
486 Neuronal GFP (yellow) and neuropil (nc82, blue) are labelled. A dashed white line
487 highlights the x-z plane imaged. **(b)** Coronal section of the thoracic cervical connective
488 in an animal expressing GCaMP6s and tdTomato in A1 neurons (*A1>GCaMP6s*;
489 *tdTomato*). Scale bar is 5 μ m. **(c)** Separated ROIs (**top-left**) and associated
490 fluorescence signals from left and right A1 neurons (**top-right**). Corresponding rotations
491 of the spherical treadmill are shown on the bottom-right. Events are indicated as dashed
492 gray and red lines for left and right A1 neuron events, respectively. **(d)** Summary of A1
493 neural activity and spherical treadmill rotations with respect to left A1 neuron
494 fluorescence events aligned to 0 s (dashed gray line). **(e)** Summary of A1 neural activity
495 and spherical treadmill rotations with respect to right A1 neuron fluorescence events
496 aligned to 0 s (dashed gray line). Control data in which events are time-shuffled are
497 overlaid in grey. Shown are the means (solid line) and bootstrapped 95% confidence
498 intervals (transparencies).



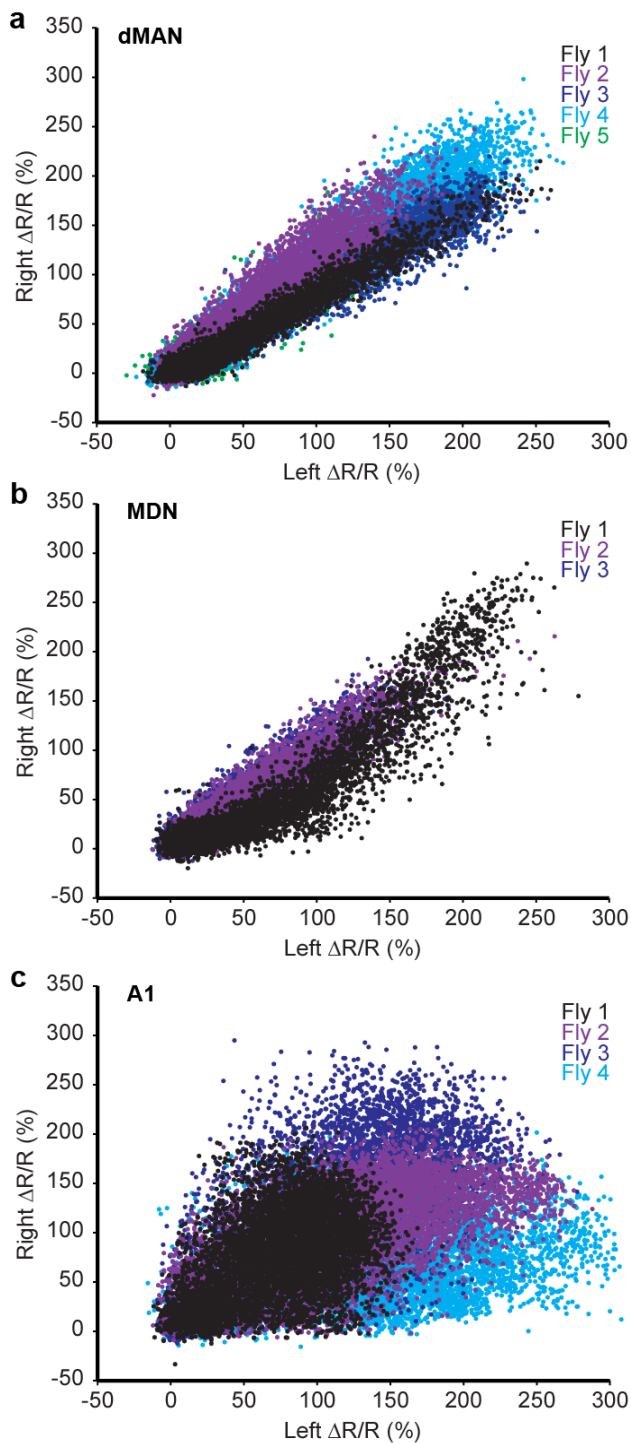
499

500 **Figure 6 | Indirect flight muscles in control and *Act88F:Rpr* animals.** Confocal
501 images of dorsal longitudinal IFMs (DLIMs) stained with TRITC-phalloidin at 1 dpe (**left**),
502 7 dpe (**right**), or wholemount confocal micrographs of myofibrillar structure (**middle**) for
503 **(a)** wild-type, or **(b)** *Act88F:Rpr* heterozygous flies. Scale bars are 5 μm.

504 **Supplementary Figures**



506 **Supplementary Figure 1 | System for VNC imaging. (a)** Photograph of the spherical
507 treadmill system and **(b)** schematic of the custom fly holder used in this study.



508

509 **Supplementary Figure 2 | Covariance in fluorescence signals between bilateral**
510 **pairs of neurons.** Scatter plots comparing $\% \Delta R/R$ signals for left and right **(a)** dMAN,
511 **(b)** MDN, or **(c)** A1 neuron pairs. Data from each animal are color-coded.

512

513 **Supplementary Videos**

514 **Supplementary Video 1 | Extent of VNC imaging volume.** 2-photon imaging of
515 horizontal sections across the dorsal-ventral extent of the VNC and cervical connective.
516 GCaMP6s (cyan) and tdTomato (red) are expressed throughout the nervous system
517 (*GMR57C10>GCaMP6s; tdTomato*). Imaging depth is indicated on the top-left.

518

519 **Supplementary Video 2 | Horizontal VNC imaging.** 2-photon imaging of a single
520 horizontal section of the VNC in a walking and grooming fly. GCaMP6s (cyan) and
521 tdTomato (red) are expressed throughout the nervous system (*GMR57C10>GCaMP6s;*
522 *tdTomato*). Shown are synchronized raw fluorescence images (**top-left**), $\% \Delta F/F$ images
523 (**top-right**), behavior images (**bottom-left**), and spherical treadmill rotations along the
524 anterior-posterior ('AP'), medial-lateral ('ML'), and yaw axes (**bottom-right**).
525 Experimenter-administered air puffs are indicated by the appearance of red boxes
526 above behavior video images. Video is 4X faster than real-time.

527

528 **Supplementary Video 3 | Coronal VNC imaging.** 2-photon imaging of a single coronal
529 section of the VNC in a walking fly. GCaMP6s (cyan) and tdTomato (red) are expressed
530 throughout the nervous system (*GMR57C10>GCaMP6s; tdTomato*). Shown are
531 synchronized raw fluorescence images (**top-left**), $\% \Delta F/F$ images (**top-right**), behavior
532 images (**bottom-left**), and spherical treadmill rotations along the anterior-posterior
533 ('AP'), medial-lateral ('ML'), and yaw axes (**bottom-right**). Video is 4X faster than real-
534 time.

535

536 **Supplementary Video 4 | Coronal cervical connective imaging.** 2-photon imaging of
537 a single coronal section of the cervical connective in a walking fly. GCaMP6s (cyan) and
538 tdTomato (red) are expressed throughout the nervous system (*GMR57C10>GCaMP6s;*
539 *tdTomato*). Shown are synchronized raw fluorescence images (**top-left**), $\% \Delta F/F$ images
540 (**top-right**), behavior images (**bottom-left**), and spherical treadmill rotations along the

541 anterior-posterior ('AP'), medial-lateral ('ML'), and yaw axes (**bottom-right**). Video is 4X
542 faster than real-time.

543

544 **Supplementary Video 5 | Coronal cervical connective imaging of dorsal**
545 **Moonwalker Ascending Neurons.** 2-photon imaging of a single coronal section of the
546 cervical connective in a behaving fly. GCaMP6s (cyan) and tdTomato (red) are
547 expressed in MANs (*MAN>GCaMP6s; tdTomato*). Raw fluorescence images of the left
548 and right dMANs are presented and outlined by ROIs (**top-left**). These images are used
549 to calculate $\% \Delta R/R$ traces for each neuron (**top-right**). Corresponding behavior
550 videography (**bottom-left**) and spherical treadmill rotations along the anterior-posterior
551 ('AP'), medial-lateral ('ML'), and yaw axes (**bottom-right**) are shown.

552

553 **Supplementary Video 6 | Behavioral responses associated with dorsal**
554 **Moonwalker Ascending Neuron activity events.** Three example behaviors (rows) for
555 each of three flies (columns) produced at the onset of dMAN fluorescence events. Red
556 square indicates the time of each fluorescence event ($t = 0$ s). Video is 3X slower than
557 real-time.

558

559 **Supplementary Video 7 | Coronal cervical connective imaging of Moonwalker**
560 **Descending Neurons.** 2-photon imaging of a single coronal section of the cervical
561 connective in a behaving fly. GCaMP6s (cyan) and tdTomato (red) are expressed in
562 MDNs (*MDN-1>GCaMP6s; tdTomato*). Raw fluorescence images of the left and right
563 MDNs are presented and outlined by ROIs (**top-left**). These images are used to
564 calculate $\% \Delta R/R$ traces for each neuron (**top-right**). Corresponding behavior
565 videography (**bottom-left**) and spherical treadmill rotations along the anterior-posterior
566 ('AP'), medial-lateral ('ML'), and yaw axes (**bottom-right**) are shown.

567

568 **Supplementary Video 8 | Behavioral responses associated with Moonwalker**
569 **Descending Neuron activity events.** Three example behaviors (rows) for each of

570 three flies (columns) produced at the onset of MDN fluorescence events. Red square
571 indicates the time of each fluorescence event ($t = 0$ s). Video is 3X slower than real-
572 time.

573

574 **Supplementary Video 9 | Coronal cervical connective imaging of A1 Neurons.** 2-
575 photon imaging of a single coronal section of the cervical connective in a behaving fly.
576 GCaMP6s (cyan) and tdTomato (red) are expressed in A1 neurons (*A1>GCaMP6s*;
577 *tdTomato*). Raw fluorescence images of the left and right A1 neurons are presented and
578 outlined by ROIs (**top-left**). These images are used to calculate $\% \Delta R/R$ traces for each
579 neuron (**top-right**). Corresponding behavior videography (**bottom-left**) and spherical
580 treadmill rotations along the anterior-posterior ('AP'), medial-lateral ('ML'), and yaw axes
581 (**bottom-right**) are shown. Video is 2X faster than real-time.

582

583 **Supplementary Video 10 | Behavioral responses associated with left A1 neuron**
584 **activity events.** Three example behaviors (rows) for each of three flies (columns)
585 produced at the onset of left A1 neuron fluorescence events. Red square indicates the
586 time of each fluorescence event ($t = 0$ s). Video is 3X slower than real-time.

587

588 **Supplementary Video 11 | Behavioral responses associated with right A1 neuron**
589 **activity events.** Three example behaviors (rows) for each of three flies (columns)
590 produced at the onset of right A1 neuron fluorescence events. Red square indicates the
591 time of each fluorescence event ($t = 0$ s). Video is 3X slower than real-time.

592 References

- 593 1. Wosnitza, A., Bockemühl, T., Dübbert, M., Scholz, H. & Büschges, A. Inter-leg
594 coordination in the control of walking speed in *Drosophila*. *The Journal of*
595 *Experimental biology* **216**, 480–491 (2013).
596
- 597 2. Mendes, C. S., Bartos, I., Akay, T., Márka, S. & Mann, R. S. Quantification of gait
598 parameters in freely walking wild type and sensory deprived *Drosophila*
599 *melanogaster*. *eLife* **2**, (2013).
600
- 601 3. Niven, J. E. Visuomotor control: *Drosophila* bridges the gap. *Curr Biol* **20**, R309–
602 11 (2010).
603
- 604 4. Card, G. M. & Dickinson, M. H. Visually mediated motor planning in the escape
605 response of *Drosophila*. *Current Biology* **18**, 1300–1307 (2008).
606
- 607 5. Pavlou, H. J. & Goodwin, S. F. Courtship behavior in *Drosophila melanogaster*.
608 towards a ‘courtship connectome’. *Curr Opin Neurobiol* **23**, 76–83 (2013).
609
- 610 6. Zwarts, L., Versteven, M. & Callaerts, P. Genetics and neurobiology of aggression
611 in *Drosophila*. *fly* **6**, 35–48 (2012).
612
- 613 7. Seeds, A. M. *et al.* A suppression hierarchy among competing motor programs
614 drives sequential grooming in *Drosophila*. *eLife* **3**, (2014).
615
- 616 8. Mann, K. J., Gordon, M. D. & Scott, K. A pair of interneurons influences the
617 choice between feeding and locomotion in *Drosophila*. **79**, 754–765 (2013).
618
- 619 9. Trimarchi, J. R. & Murphey, R. K. The shaking-B-2 mutation disrupts electrical
620 synapses in a flight circuit in adult *Drosophila*. *J Neurosci* **17**, 4700–4710 (1997).
621
- 622 10. Ikeda, K. & Kaplan, W. D. Neurophysiological Genetics in *Drosophila*
623 *melanogaster*. *American Zoologist* **14**, 1055–1066 (1974).
624
- 625 11. Tuthill, J. C. & Wilson, R. I. Parallel Transformation of Tactile Signals in Central
626 Circuits of *Drosophila*. *Cell* **164**, 1046–1059 (2016).
627
- 628 12. Hedwig, B. & Burrows, M. Presynaptic inhibition of sensory neurons during kicking
629 movements in the locust. *J Neurophysiol* **75**, 1221–1232 (1996).
630
- 631 13. Bässler, U. & Büschges, A. Pattern generation for stick insect walking
632 movements—multisensory control of a locomotor program. *Brain Research*
633 *Reviews* **27**, 65–88 (1998).
634
- 635 14. Maimon, G., Straw, A. D. & Dickinson, M. H. Active flight increases the gain of
636 visual motion processing in *Drosophila*. *Nat Neurosci* **13**, 393–399 (2010).
637

- 638 15. Chen, T.-W. *et al.* Ultrasensitive fluorescent proteins for imaging neuronal activity.
639 *Nature* **499**, 295–300 (2013).
640
- 641 16. Shaner, N. *et al.* Improved monomeric red, orange and yellow fluorescent proteins
642 derived from *Discosoma sp.* red fluorescent protein. *Nature Biotechnology* **22**,
643 1567–1572 (2004).
644
- 645 17. Jenett, A. *et al.* A GAL4-Driver Line Resource for *Drosophila* Neurobiology. *Cell*
646 *Reports* **2**, 991–1001 (2012).
647
- 648 18. Seelig, J. D. *et al.* Two-photon calcium imaging from head-fixed *Drosophila* during
649 optomotor walking behavior. *Nature Methods* **7**, 535–540 (2010).
650
- 651 19. Hedwig, B. & Poulet, J. Complex auditory behaviour emerges from simple
652 reactive steering. *Nature* **430**, 781–785 (2004).
653
- 654 20. Tsubouchi, A. *et al.* Topological and modality-specific representation of
655 somatosensory information in the fly brain. *Science* **358**, 615–623 (2017).
656
- 657 21. Enriquez, J. *et al.* Specification of Individual Adult Motor Neuron Morphologies by
658 Combinatorial Transcription Factor Codes. *Neuron* **86**, 955–970 (2015).
659
- 660 22. Namiki, S., Dickinson, M. H., Wong, A. M., Korff, W. & Card, G. M. The functional
661 organization of descending sensory-motor pathways in *Drosophila*. *bioRxiv* 1–67
662 (2017).
663
- 664 23. Bidaye, S. S., Machacek, C., Wu, Y. & Dickson, B. J. Neuronal control of
665 *Drosophila* walking direction. *Science* **344**, 97–101 (2014).
666
- 667 24. Sen, R. *et al.* Moonwalker Descending Neurons Mediate Visually Evoked Retreat
668 in *Drosophila*. *Curr Biol* **27**, 766–771 (2017).
669
- 670 25. Luan, H., Peabody, N. C., Vinson, C. R. & White, B. H. Refined Spatial
671 Manipulation of Neuronal Function by Combinatorial Restriction of Transgene
672 Expression. **52**, 425–436 (2006).
673
- 674 26. White, K. *et al.* Genetic Control of Programmed Cell Death in *Drosophila*. *Science*
675 **264**, 677–683 (1994).
676
- 677 27. Ramdya, P., Schaffter, T., Floreano, D. & Benton, R. Fluorescence Behavioral
678 Imaging (FBI) Tracks Identity in Heterogeneous Groups of *Drosophila*. *PLoS One*
679 **7**, e48381 (2012).
680
- 681 28. Reedy, M. C., Bullard, B. & Vigoreaux, J. O. Flightin is essential for thick filament
682 assembly and sarcomere stability in *Drosophila* flight muscles. *J. Cell Biol.* **151**,
683 1483–1499 (2000).

- 684
685 29. Robie, A. A. *et al.* Mapping the Neural Substrates of Behavior. *Cell* **170**, 393–406
686 (2017).
687
688 30. Harris, R. M., Pfeiffer, B. D., Rubin, G. M. & Truman, J. W. Neuron hemilineages
689 provide the functional ground plan for the *Drosophila* ventral nervous system.
690 *eLife* **4**, (2015).
691
692 31. Markstein, M., Pitsouli, C., Villalta, C., Celniker, S. E. & Perrimon, N. Exploiting
693 position effects and the gypsy retrovirus insulator to engineer precisely expressed
694 transgenes. *Nat Genet* **40**, 476–483 (2008).
695
696 32. Nongthomba, U. & Ramachandra, N. B. A direct screen identifies new flight
697 muscle mutants on the *Drosophila* second chromosome. *Genetics* **153**, 261–274
698 (1999).
699
700 33. Viswanathan, M. C., Blice-Baum, A. C., Schmidt, W., Foster, D. B. & Cammarato,
701 A. Pseudo-acetylation of K326 and K328 of actin disrupts *Drosophila*
702 *melanogaster* indirect flight muscle structure and performance. *Front Physiol* **6**,
703 116 (2015).
704
705 34. Schindelin, J. *et al.* Fiji: An open-source platform for biological-image analysis.
706 *Nature Methods* **9**, 676–682 (2012).
707
708 35. Weir, P. T. *et al.* Anatomical Reconstruction and Functional Imaging Reveal an
709 Ordered Array of Skylight Polarization Detectors in *Drosophila*. *Journal of*
710 *Neuroscience* **36**, 5397–5404 (2016).
711
712 36. Fayyazuddin, A. & Dickinson, M. H. Haltere afferents provide direct, electrotonic
713 input to a steering motor neuron in the blowfly, *Calliphora*. *J Neurosci* **16**, 5225–
714 5232 (1996).
715
716 37. Horn, B. & Schunck, B. G. Determining Optical-Flow. *Artificial intelligence* **17**,
717 185–203 (1981).
718
719 38. Brox, T., Bruhn, A., Papenbergh, N. & Weickert, J. High accuracy optical flow
720 estimation based on a theory for warping. *Computer Vision - Eccv 2004, Pt 4*
721 **2034**, 25–36 (2004).
722
723 39. Revaud, J., Weinzaepfel, P., Harchaoui, Z. & Schmid, C. DeepMatching:
724 Hierarchical Deformable Dense Matching. *Int J Comput Vis* **120**, 300–323 (2016).
725
726 40. Boyd, S., Parikh, N., Chu, E., Peleato, B. & Eckstein, J. Distributed optimization
727 and statistical learning via the alternating direction method of multipliers.
728 *Foundations and Trends in Machine Learning* **3**, 1–122 (2010).
729

- 730 41. Unser, M., Soubies, E., Soulez, F., McCann, M. & Donati, L. GlobalBiolm: A
731 unifying computational framework for solving inverse problems. in CTu1B.1 (OSA,
732 2017).
733
- 734 42. Sun, D., Roth, S. & Black, M. J. A quantitative analysis of current practices in
735 optical flow estimation and the principles behind them. *Int J Comput Vis* **106**, 115–
736 137 (2014).
737
- 738 43. Guizar-Sicairos, M., Thurman, S. T. & Fienup, J. R. Efficient subpixel image
739 registration algorithms. *Opt Lett* **33**, 156–158 (2008).
740
- 741 44. Weir, P. T. & Dickinson, M. H. Functional divisions for visual processing in the
742 central brain of flying *Drosophila*. *Proc Natl Acad Sci USA* **112**, E5523–32 (2015).
743
- 744 45. Ikegaya, Y. *et al.* Synfire chains and cortical songs: temporal modules of cortical
745 activity. *Science* **304**, 559–564 (2004).
746